

A combined experimental/theoretical investigation of the near-infrared photodissociation of $\text{IBr}^-(\text{CO}_2)_n$

Matthew A. Thompson,^{a)} Joshua P. Martin, Joshua P. Darr, W. Carl Lineberger,^{b)} and Robert Parson^{c)}

JILA and Department of Chemistry and Biochemistry, University of Colorado, Boulder, Colorado 80309-0440, USA

(Received 23 September 2008; accepted 4 November 2008; published online 9 December 2008)

We report the collaborative experimental and theoretical study of the time-resolved recombination dynamics of photodissociated $\text{IBr}^-(\text{CO}_2)_n$ clusters. Excitation of the bare anionic chromophore to the dissociative $A' \ ^2\Pi_{1/2}$ state yields only I^- and Br^- products. Interestingly, however, the addition of a few solvent molecules promotes recombination of the dissociating chromophore on the $X \ ^2\Sigma_{1/2}^+$ ground state, which correlates asymptotically with Br^- and I^- products. This process is studied experimentally using time-resolved, pump-probe techniques and theoretically via nonadiabatic molecular dynamics simulations. In sharp contrast to previous I_2^- studies where more kinetic energy was released to the photofragments, the observed recombination times increase from picoseconds to nanoseconds with increasing cluster size up to $n=10$. The recombination times then drop dramatically back to picoseconds for cluster sizes $n=11-14$. This trend, seen both in experiment and theory, is explained by the presence of a solvent-induced well on the A' state, the depth of which directly corresponds to the asymmetry of the solvation about the chromophore. The results seen for both the branching ratios and recombination times from experiment and theory show good qualitative agreement. © 2008 American Institute of Physics. [DOI: 10.1063/1.3033746]

I. INTRODUCTION

The study of ultrafast cluster dynamics has long been a field of interest allowing for the investigation of the behavior of molecules influenced by their environments.^{1,2} Simplification of the local environment by using gas phase cluster ions provides one the chance to study these influences and gain a fundamental understanding of the effects solvation has on molecules.^{1,3-5} These effects can be seen in simple processes such as solvent molecules being used to dissipate energy or more complex interactions involving perturbation of the electronic character of the solvated chromophore. Phenomena resulting from solvent perturbed potential energy surfaces, such as solvent-induced recombination and “cage effects,” can be studied using molecular dynamics (MD) with the application of simple, first-order kinetic models.

In simple first-order kinetic models such as these, branching ratios and rate constants usually track one another.⁶ When a chemical reaction can proceed through parallel channels to distinct final products, one usually expects that the faster channels will have higher overall product yields. Any other result suggests a more complicated underlying mechanism, one in which branching and overall rate are controlled by different processes.

For the past 15 years, we have carried out a collaborative theoretical and experimental investigation into the dynamics of photodissociation of diatomic molecular ions embedded in

mass-selected molecular clusters.⁷⁻¹⁷ A common theme that runs through much of this work has been the systematic measurement of cluster size dependence of product branching ratios, such as the relative probabilities of dissociation versus solvent-induced recombination, and of the time constants for the associated processes. This paper is the third in a series^{18,19} devoted to experimental and theoretical investigations of photodissociation and recombination of IBr^- anions embedded in clusters of 1–16 CO_2 molecules. The second paper in this series reported¹⁸ a surprising disparity between the overall propensity for solvent-induced recombination following near-infrared (IR) excitation and the rate of this recombination process. For example, as the number of CO_2 solvents around IBr^- was increased from 5 to 8, the recombination probability increased¹⁹ from 90% to 100%, but the timescale for recombination increased from 12 to 900 ps.¹⁸ This result is in dramatic variance with earlier investigations of the homonuclear dihalide cluster $\text{I}_2^-(\text{CO}_2)_n$, where somewhat more kinetic energy was available to the photofragments and for which recombination times were of the order of 10 ps and decreased with increasing cluster size.^{10,12} The results of nonadiabatic MD simulations, which reproduced these experimental trends, were also included in the earlier papers.^{13,14,16,17} On the basis of the $\text{IBr}^-(\text{CO}_2)_n$ simulations, it was predicted that the trend in recombination time would reverse as the cluster size was increased further.

In the course of this collaboration, experiment and simulation¹³⁻¹⁷ have proceeded in parallel. On multiple occasions, preliminary results from one track have influenced the decisions made in implementing the other. The form and content of this paper and its predecessors reflect this close

^{a)}Present address: Code 6189, Theoretical Chemistry Section, Naval Research Laboratory, Washington, DC 20375.

^{b)}Electronic mail: wcl@jila.colorado.edu.

^{c)}Electronic mail: rparson@jila.colorado.edu.

degree of interaction—rather than sequester the simulations and the experiments in separate papers, we have included some of each in each publication, with the relative emphasis changing from one to another. The preceding paper¹⁸ was primarily experimental, with the simulation results, together with a brief discussion of their interpretation, included in order to lend credence to and better illuminate the significance of the surprising experimental trends. The present paper incorporates a much more complete description of the details of the simulation methodology and of the analysis of the simulation results, together with new experimental results which confirm the predictions made in the previous paper.

The paper is laid out as follows. Section II summarizes briefly the experimental setup and the method used to determine the recombination times and then describes in more detail the simulation model, with particular attention to those features that distinguish it from that used for earlier simulations of $I_2^-(CO_2)_n$.²⁰ Section III begins with a presentation of those simulation results that can be directly compared to experiment: recombination probabilities, absorption recovery curves, and the dependence of the recombination time on cluster size. New experimental results, recombination times for clusters with $n > 10$, are also included in this portion. The remainder of Sec. III deals with the analysis and interpretation of the simulation trajectories. The principal analysis tool is a collective “solvent coordinate,” adopted from earlier work²¹ on I_2^- , which describes the extent to which the solvent stabilizes a charge on one atom of the diatomic chromophore relative to the other. As in previous work,¹⁷ the trajectory ensembles are found to organize themselves into distinctive patterns when analyzed in this way. Section IV is devoted to organizing these patterns into a simple, yet comprehensive mechanistic picture of the recombination process that explains the major experimental trends. It is argued that the rate-determining step in recombination is an adiabatic electron transfer process in which both the electronic charge and the solvent cage move in concert from the Br to the I atom. Section V summarizes the experimental and theoretical findings and their interpretation.

II. METHODS

A. Experimental apparatus

The experimental apparatus utilized for the study of $IBr^-(CO_2)_n$ cluster anion dynamics has been previously described²² in detail; therefore, only a brief description will be presented here. The anions are formed following electron impact ionization of a pulsed supersonic expansion of a gas mixture obtained by passing dry CO_2 (2–3 atm) over solid IBr (Aldrich, 98% pure) at room temperature. The source of the pulsed expansion is a series 9 General Valve with a 0.8 mm orifice, operated at 100 Hz. The expanding gas mixture encounters a 250 μA , 1 keV electron beam, oriented collinear to the pulsed expansion, producing slow secondary electrons that attach to neutral IBr. Solvent molecules subsequently attach to the IBr^- chromophore to form the desired $IBr^-(CO_2)_n$ cluster anions. Based on estimates utilizing an

evaporative ensemble model, the cluster anions have an internal energy corresponding to 150–60 K, decreasing with increasing cluster size.^{23,24}

Anions are extracted perpendicularly into a Wiley–McLaren time-of-flight (TOF) mass spectrometer²⁵ via an ≈ 1 kV pulse. Upon entering the TOF, the ions are further accelerated to ≈ 3 keV. Ion optics steer and focus the anions to a spatial focus at the laser interaction region, 1.8 m downstream. A mass gate immediately before the laser interaction region allows for selection of a specified cluster size. The selected cluster anions are then excited with a 795 nm pump beam, followed by a temporally delayed 795 nm probe beam. The ionic photoproducts enter a secondary reflectron mass analyzer, where they are separated according to mass before detection using a microchannel plate detector operated in ion counting mode.

1. Laser system

The ultrafast laser system utilized in the measurement of the absorption recovery times of $IBr^-(CO_2)_n$ clusters has been described in a recent publication.¹⁸ In brief, the femtosecond laser system begins with a Coherent Mira 900-B Ti:sapphire oscillator pumped by a Coherent Verdi V5 neodymium vanadate solid state laser. The output beam is then amplified in a Quantronix Titan regenerative/multipass Ti:sapphire amplifier pumped by the 527 nm output of a Quantronix neodymium yttrium lithium fluoride laser to produce 3 mJ, ≈ 140 fs, 795 nm pulses at a 400 Hz repetition rate. This beam is split with 60% of the energy going into the pump pulse and the remaining 40% into the probe pulse. The pump beam passes through a computer-controlled, precision variable delay stage (≈ 100 fs resolution) with an 800 ps range, allowing for the measurement of fast recovery times. Measuring long recovery times is achieved by sending the probe beam through a manual delay stage with an accuracy of ≈ 20 ps, providing delay times up to a maximum of 3.5 ns.

2. Methodology

A one-color (795 nm) pump-probe scheme is employed to measure the absorption recovery times for the $IBr^-(CO_2)_n$ cluster anions.¹⁸ Photoexcitation of the bare anionic dihalide at this wavelength exclusively excites the chromophore to the $A' \ ^2\Pi_{1/2}$ state, leading to $I^- + Br$ products with 0.285 eV kinetic energy release. As CO_2 solvent molecules are added, the ionic photoproducts change to Br^- - and IBr^- -based products with varying degrees of solvation, indicating dissociation on the ground-state surface or recombination of the chromophore, respectively.¹⁹ With eight or more solvent molecules attached to the chromophore, the only observed photoproducts are IBr^- based, indicating 100% recombination.¹⁹ Once recombined and sufficiently vibrationally relaxed on the ground state, the clusters regain near-IR absorption and can again be excited to the $A' \ ^2\Pi_{1/2}$ state via the 795 nm probe pulse. Following the absorption of a second photon, the ionic photoproducts have a mass-to-charge ratio different from any of the one-photon products. Two-photon products are then monitored as a function of

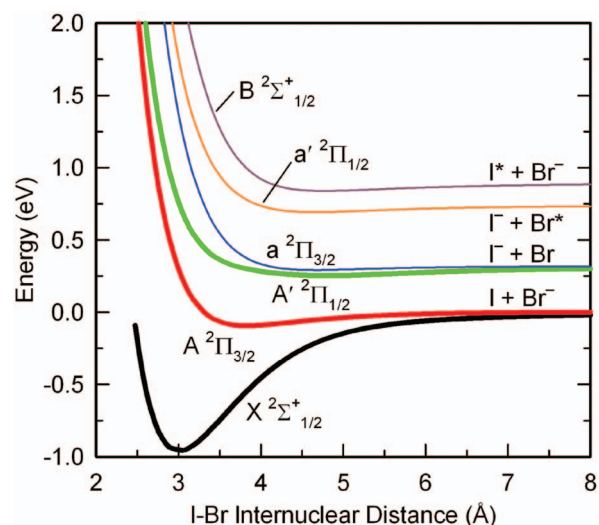


FIG. 1. (Color) Potential energy curves for the six lowest spin-orbit states of IBr^- .

pump-probe delay time, taking advantage of the fact that the secondary reflectron mass spectrometer can be adjusted to detect only products of pump and probe laser absorption.¹⁸ Appropriate background corrections are applied to assure that the reported two-photon signal results only from the absorption of one photon from each of the pump and probe laser pulses.^{10,24,26} In the work reported here, this procedure is carried out on $\text{IBr}^-(\text{CO}_2)_{11-14}$ cluster anions to measure their absorption recovery times.

B. Electronic structure

The potential energy curves, Fig. 1, and associated electronic properties of the isolated IBr^- solute are obtained using MOLPRO 2002.²⁷ The energy-consistent effective core potential (ECP) of Stoll *et al.*²⁸ is used, specifically, the large-core ECPs, which are based on multiconfigurational Dirac-Hartree-Fock (MDF) calculations of the neutral atom and the associated core polarization potentials, which model the charge-induced dipole interaction of the core. The basis sets are an augmented form, $(7s7p3d2f)/[5s5p3d2f]$, of the stock $(6s6p)/[4s4p]$ basis sets included with the ECPnMDF core potentials.^{28,29} The augmented basis provides superior electron affinity performance compared to the stock basis with little additional calculation time.

The electronic structure calculations use the internally contracted multireference configuration interaction methods developed by Knowles and Werner.³⁰⁻³² The reference orbitals and configurations are obtained from state-averaged complete active-space self-consistent field calculations^{33,34} that consist of 15 electrons in the lowest two Σ , Π_x , and Π_y states that arise from the 2P state of the neutral and 1S state of the ion. A spin-orbit calculation of all six states is then performed using spin-orbit ECPs.³⁵ This is in contrast to earlier calculations²⁰ of I_2^- and ICl^- which relied on a semiempirical treatment of spin-orbit coupling. The calculation is performed at 42 points along the potential energy surface corresponding to bond lengths ranging from $4.5a_0$ to $100a_0$, and cubic splines are used to interpolate between the points. R_e

TABLE I. Summary of energetics from *ab initio* calculations (energies in eV).

		Calc.	Expt.	$\Delta(\text{Calc.}-\text{Expt.})$
Spin-orbit splitting	Br	0.4237	0.4569 ^a	-0.0331
	I	0.8932	0.9427 ^a	-0.0495
	ΔEA^b	0.3156	0.3045 ^c	0.0111
			1.10(4) ^d	-0.152
	$D_0(\text{IBr}^-)$	0.948 ^e		
			0.954(6) ^f	-0.006
	$\text{EA}(\text{IBr})$:	2.494	2.51(1) ^f	-0.016
	R_e (Å):	3.05	3.06(3) ^f	-0.01

^aReference 50.

^bElectron affinity difference between I and Br.

^cReference 51.

^dReference 19.

^eCalculated using $\omega_e=118\text{ cm}^{-1}$, as obtained by analysis of the ground-state potential energy curve with LeRoy's LEVEL program, Ref. 52.

^fPreliminary results, Ref. 53.

and D_e of the ground electronic state shown in Fig. 1 are 3.05 Å and 0.96 eV, respectively. Other electronic properties of IBr^- may be found in Table I.

C. Molecular dynamics

The nonadiabatic MD simulations for $\text{IBr}^-(\text{CO}_2)_n$ are based on the effective Hamiltonian method developed by Maslen *et al.*³⁶ and previously applied^{15-17,37,38} to $\text{I}_2^-(\text{CO}_2)_n$. Briefly, the electrostatic and induction interactions between the IBr^- solute and the CO_2 solvent are calculated from an operator including electrostatic and induction terms for the solute and solvent. For the solute, a distributed multipole analysis (DMA) (Ref. 39) of the isolated solute electronic structure is calculated. The diagonal terms of the DMA describe the charge distribution associated with each solute electronic state, while the off-diagonal terms (distributed transition moment) allow the solute charge to be polarized by the electric fields generated by the solvent charge distribution. The multipoles are distributed among four sites, one at each nucleus and two equidistant points along the bond axis. The distributed multipoles, along with nonadiabatic coupling matrix energy elements and transition angular momenta, are calculated and interpolated on the same grid as the energies above. The solvent charge distribution and polarizabilities and the solvent-solute interactions are obtained from a condensed-phase model.⁴⁰ The short-range dispersion-repulsion interactions between solute and solvent are described by atom-atom Lennard-Jones potentials, with parameters calculated from high resolution photoelectron spectra⁴¹ and from fits of coupled cluster (CCSD) calculations of the $\text{Br}^- \cdots \text{CO}_2$ interactions.

At each time step of a MD simulation, the effective Hamiltonian for the solvated ion is diagonalized to yield the energies, forces, and nonadiabatic transition probabilities needed for the next step. On a single state, motion is computed using the velocity Verlet algorithm,⁴² while nonadiabatic transitions are performed according to a modified¹⁶ version of Tully's fewest-switches surface-hopping method.^{43,44}

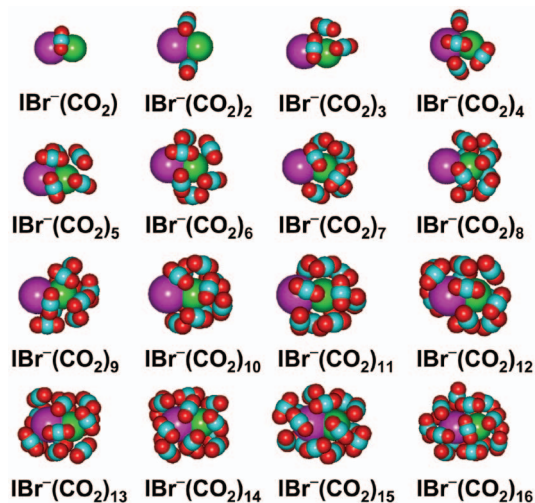


FIG. 2. (Color) Exemplar calculated minimum energy structures for $\text{IBr}^-(\text{CO}_2)_n$, $n=1-16$. The pattern of CO_2 filling is first around the bond, next the Br end at $n=3$, and then the I end at $n=9$.

D. Minimum energy structures

Minimum energy structures for $\text{IBr}^-(\text{CO}_2)_n$ ($n=1-16$) are constructed by sampling 201 configurations from a 1 ns trajectory on the IBr^- ground state having an energy corresponding to a temperature of 80 K. These configurations are then quenched to local minima using Newton–Raphson minimization.⁴⁵ The lowest energy structure obtained for each cluster size is shown in Fig. 2, and the energetic properties are reported in Table II. While this procedure is not expected to find the lowest energy configuration for any but the smallest clusters, the structures reported in Fig. 2 and Table II are certainly characteristic of the minimum energy configurations of the cluster anions. To quantify the energetics, we define a sequential binding energy (SBE),

TABLE II. Properties of minimal energy clusters of $\text{IBr}^-(\text{CO}_2)_n$ from 80 K trajectory ensembles.

n	PE (meV) ^a	Δ_n (meV) ^b	$-PE/n$ (meV)	No. of local minima
1	-205	205	205	1
2	-406	201	203	23
3	-627	222	209	22
4	-852	225	213	47
5	-1074	222	215	65
6	-1301	227	217	98
7	-1525	224	218	104
8	-1775	251	222	63
9	-2009	233	223	64
10	-2248	240	225	112
11	-2483	234	226	135
12	-2680	198	223	111
13	-2917	237	224	126
14	-3157	240	225	143
15	-3380	223	225	131
16	-3588	208	224	140

^aNot including IBr^- bond energy (0.956 eV).

^bSee Eq. (1).

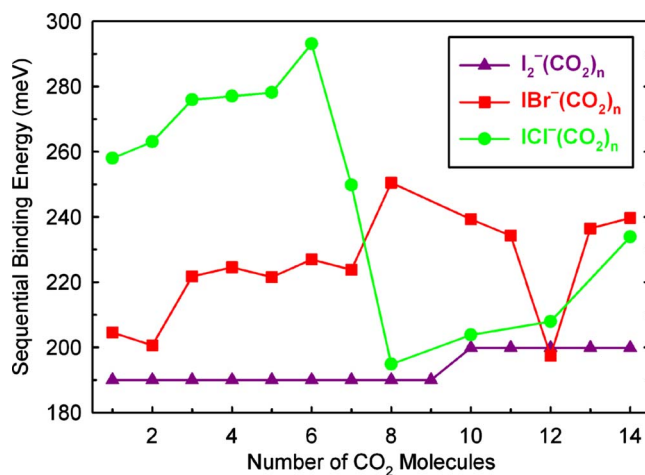


FIG. 3. (Color online) Sequential binding energies for calculated minimum energy clusters of $\text{IBr}^-(\text{CO}_2)_n$ (squares), $\text{ICl}^-(\text{CO}_2)_n$ (circles), and $\text{I}_2^-(\text{CO}_2)_n$ (triangles).

$$\Delta_n = \text{PE}_{n-1} - \text{PE}_n, \quad (1)$$

where PE_n is the potential energy of the cluster with n solvent molecules. Figure 3 compares the SBEs of $\text{IBr}^-(\text{CO}_2)_n$, $\text{ICl}^-(\text{CO}_2)_n$, and $\text{I}_2^-(\text{CO}_2)_n$.

For $\text{I}_2^-(\text{CO}_2)_n$,⁴⁶ the solvation occurs around a symmetric, homonuclear diatomic molecule and each CO_2 molecule that is added around the I_2^- chromophore lowers the potential energy of the cluster by essentially the same amount. For $\text{ICl}^-(\text{CO}_2)_n$,⁴⁷ however, there is a large size difference between the two atoms of the molecule. Initial solvation then occurs around the smaller Cl end of the chromophore due to the stronger Cl^- -solvent interaction compared with the I^- -solvent interaction. As the number of CO_2 solvent molecules increases, the SBE increases until the Cl end of the chromophore is completely solvated. At this point in the solvation, any further increase in the number of CO_2 molecules initiates solvation around the I end of the chromophore, causing a drastic reduction in the SBE. This is clearly seen in Fig. 3 as the number of CO_2 molecules solvating ICl^- increases from 6 to 8.

Comparing $\text{IBr}^-(\text{CO}_2)_n$ to $\text{ICl}^-(\text{CO}_2)_n$ and $\text{I}_2^-(\text{CO}_2)_n$ (Fig. 3), we see that $\text{IBr}^-(\text{CO}_2)_n$ is intermediate between the other two cluster families. As can be seen in Fig. 3, for $n=1$ and 2 the SBEs of $\text{IBr}^-(\text{CO}_2)_n$ and $\text{I}_2^-(\text{CO}_2)_n$ are similar. At $n=1$, $\text{IBr}^-(\text{CO}_2)_n$ and $\text{I}_2^-(\text{CO}_2)_n$ both have one CO_2 perpendicular to the solute bond at the bond center, while for $n=2$, the second is placed opposite the first CO_2 , again perpendicular to the solute. These early SBEs also compare reasonably well to experimental estimates.^{9,19}

Beginning with $n=3$, the solvent molecules begin to exhibit some of the same trends that were observed with $\text{ICl}^-(\text{CO}_2)_n$. At $n=3$, the solvent molecules cluster around the Br end, increasing the SBE with respect to $n=1$ and 2. At $n=8$, a particularly stable half-filled solvation shell is formed with maximum interaction with bromine. This half-full solvation shell is analogous to $\text{ICl}^-(\text{CO}_2)_6$, where the maximum CO_2 interaction with chlorine occurs. Also, as observed with $\text{ICl}^-(\text{CO}_2)_n$, for larger n , the solvent molecules add to the I side, and the SBE begins to decrease again. In the case of

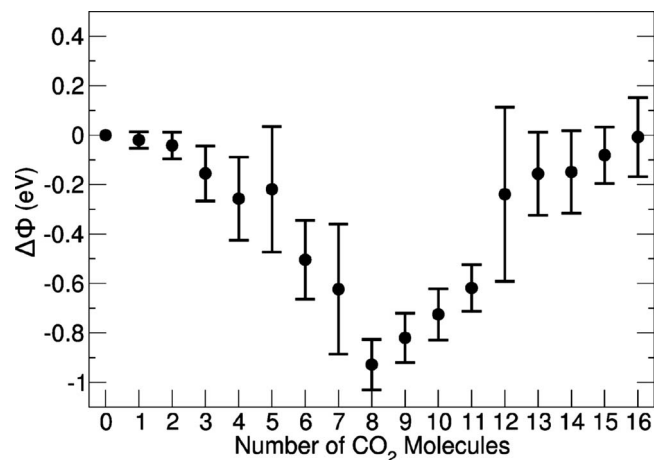


FIG. 4. Average $\Delta\Phi$ for 100 configurations of $\text{IBr}^-(\text{CO}_2)_{0-16}$ in the ground state at 60 K. Error bars represent one standard deviation of the mean.

$\text{IBr}^-(\text{CO}_2)_n$, however, this decrease is somewhat irregular. In particular, $\text{IBr}^-(\text{CO}_2)_{12}$ has a very low SBE compared to other large clusters. This indicates that compared to both $n=11$ and $n=13$, $n=12$ does not form a particularly stable, minimum energy structure. To quantify this, we calculate the asymmetry of the solvent configuration, $\Delta\Phi$, defined as the energy required to move a charge of $-e$ from the I end to the Br end of a cluster. Negative values mean solvation favors bromine, while positive values favor iodine. Figure 4 shows that $\text{IBr}^-(\text{CO}_2)_{12}$ has a labile ground-state configuration, reflecting its less rigid solvent-shell structure and, consequently, has a relatively low SBE.

E. Trajectory methods

Ensembles for MD simulations are constructed as follows. First, starting from the calculated minimum energy structures, the cluster is warmed for 40 ps at a temperature of 60 K, followed by a 100 ps run on the ground state to test that the cluster energetics are stable. After that, the ensembles are constructed using a 2 fs time-step run on the electronic ground state that samples every 5 ps until 100 configurations are constructed.

To start the photoproduct trajectories, the configurations of the constructed ensemble have their I-Br bond lengths adjusted to match the experimental photon energy, in this case 790 nm, for near-IR excitation. Since this excitation lies in the $A' \leftarrow X$ absorption band, see Fig. 5, only small adjustments are needed, on the order of 0.1–0.2 Å. A step size of 1 fs is used for all trajectories, which results in energy conservation on the order of $10^{-3} E_h$. A trajectory is classified as “dissociated” if the solute bond length ever exceeded $40a_0$ on any electronic surface and as “recombined” if it ever became less than 3.3 Å on the ground state. As discussed in Sec. III, the timescales for recombination in the intermediate-sized clusters ($n=8-10$) are extremely long, and in these cases it is not feasible to follow every trajectory in an ensemble all the way to its final destination. In these cases, we propagate the ensemble until enough trajectories have recombined that we can calculate a recombination time—this requires as much as 2 ns in extreme cases—and

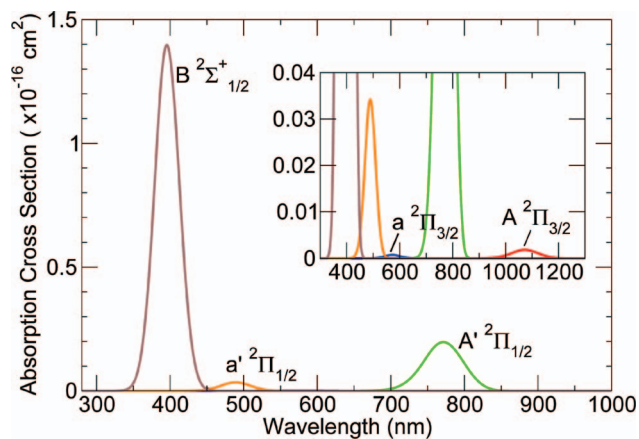


FIG. 5. (Color) Calculated photoabsorption spectrum for IBr^- .

then extrapolate the branching ratio for recombination on the basis of the fraction of trajectories that have dissociated or recombined at this time. (In other words, we assume that those trajectories which are still trapped in the excited state when the simulation is terminated have the same statistical properties as those which have reached their final state.)

III. RESULTS

A. Photofragment branching ratios

The simulated branching ratios for 790 nm excitation are shown in Fig. 6, together with the experimental results which were published previously.¹⁹ In both experiment and simulation, the uncaged (I^- -based) photoproducts disappear quickly as the size of the precursor cluster increases, although there are discrepancies at a finer level of detail—in experiment the I^- channel closes at $n=5$, while the simulations show it to be open (at a very low level) up to $n=13$. The simulations do not do as well at reproducing the branching between

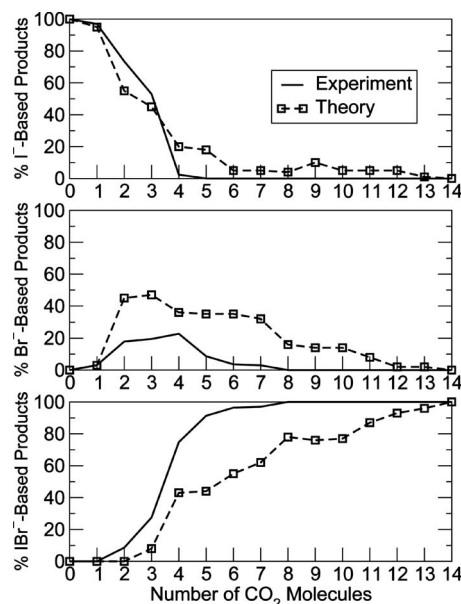


FIG. 6. Near-IR (790 nm) branching ratios for $\text{IBr}^-(\text{CO}_2)_n$. The theoretical simulated results (dashed line) are based on an “infinite” timescale. The experimental results (solid line) are from Sanford *et al.* (Ref. 19).

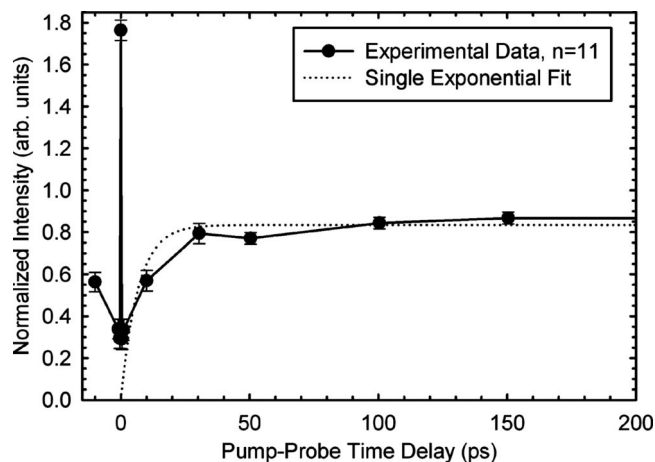


FIG. 7. Transient illustrating the absorption recovery of $\text{IBr}^-(\text{CO}_2)_{11}$. The circles represent the experimental data, and the dotted line is the result of a single exponential fit. The black line is used to guide the eye.

Br^- -based dissociated products and recombined products. This suggests that the model might underemphasize the strength of the $\text{I} \cdots \text{Br}$ interaction or, perhaps, that the solute-solvent interactions allow for too facile dissociation. Nevertheless, the simulations show a similar pattern of Br^- -product increase and decrease up to $n=7$. It is only for cluster sizes $n > 7$ that the simulation begins to differ from the experiment significantly. While the excitation wavelength employed in this simulation gives a slightly different kinetic energy release than the corresponding experiment, simulations with slightly different energy release have only a minor effect on the product branching ratios. The amount of kinetic energy release, however, has a much more significant effect on the recombination times, as discussed later.

B. Near-IR time-resolved studies

1. Experimentally observed absorption recovery dynamics of $\text{IBr}^-(\text{CO}_2)_n$, $n=11-14$

The absorption recovery times of the smaller $\text{IBr}^-(\text{CO}_2)_n$ clusters, $n=5-10$, following 795 nm excitation to the $A'^2\Pi_{1/2}$ state were previously reported by our group.¹⁸ In this work, it was found that the absorption recovery time increased as the number of CO_2 molecules in the cluster, n , increased from tens of picoseconds for $\text{IBr}^-(\text{CO}_2)_{5,6}$ to almost 1 ns for $\text{IBr}^-(\text{CO}_2)_{8,10}$. While this cluster size dependence is the opposite of that observed^{10,12,26} for $\text{I}_2^-(\text{CO}_2)_n$, $\text{I}_2^-(\text{OCS})_n$, and $\text{I}_2^-(\text{Ar})_n$, it has been corroborated by theoretical predictions. Furthermore, these predictions indicated that for even larger clusters, $n=12$ and 13 , the absorption recovery lifetime should return to tens of picoseconds as with $\text{IBr}^-(\text{CO}_2)_{5,6}$.

At that time, experimental difficulties prevented the formation of the larger ion clusters. The cluster ion production difficulties have now been resolved and experimental results for these and other larger clusters are presented here.

Figure 7 shows the time-dependent absorption recovery of $\text{IBr}^-(\text{CO}_2)_{11}$. The transient is obtained by using a weighted average of the signal resulting from four days of data acquisition of the IBr^- and $\text{IBr}^-(\text{CO}_2)$ two-photon products. Plotted individually, these two products exhibited very similar

absorption recovery transients. However, the appearance of the transients changed slightly on a day-to-day basis. The y axis in Fig. 7 represents the two-photon, pump-probe signal normalized to unity at the signal level observed at a 500 ps time delay. The transient shows a steep, initial rise from slightly greater than 0 to 30 ps and then a more gradual rise until 650 ps. While all the data sets show the steep, initial rise from 0 to 30 ps, the more gradual rise out to 650 ps is only observed in two of the four data sets. Because both the pump and probe pulses are the same wavelength, the signal is symmetric about $t=0$. When the pump and probe beams overlap temporally, we see a large “coherence peak” whose shape is essentially the autocorrelation function of the 795 nm laser pulse. When fitting the absorption recovery data, however, we avoid this artifact with the physically compelling assumption that there can be no recombination at time zero,

$$N(t) = [1 - e^{-t/\tau}], \quad (2)$$

where τ represents the absorption recovery lifetime. Fitting to this model yields a value of 7(2) ps for τ . This fit is shown in Fig. 7. The experimental data also hint at the possibility of a long recovery time for a small (possibly 10%) component of the $\text{IBr}^-(\text{CO}_2)_{11}$ clusters; however, given the day-to-day fluctuations associated with the data sets, a definitive conclusion cannot be made. Regardless of the exact functional form of the fit that is utilized, though, it is clear that the principal absorption recovery occurs much more rapidly than was observed for the $\text{IBr}^-(\text{CO}_2)_8$ and $\text{IBr}^-(\text{CO}_2)_{10}$ clusters, 900(100) ps. This result is in accord with theoretical predictions that the absorption recovery time should decrease for larger $\text{IBr}^-(\text{CO}_2)_n$ clusters.¹⁸

The $\text{IBr}^-(\text{CO}_2)_{12}$ absorption recovery dynamics are qualitatively similar to those observed for $\text{IBr}^-(\text{CO}_2)_{11}$. In this case, however, only the $\text{IBr}^-(\text{CO}_2)$ two-photon product was detected. Furthermore, no evidence was observed for a second time constant. A single exponential fit of the data yielded a lifetime of 10.3(8) ps, in further support of the theoretical predictions for the larger $\text{IBr}^-(\text{CO}_2)_n$ clusters.¹⁸

The transient depicting the absorption recovery of $\text{IBr}^-(\text{CO}_2)_{13}$ is illustrated with filled squares in Fig. 8. This transient was obtained by summing data from the $\text{IBr}^-(\text{CO}_2)$, $\text{IBr}^-(\text{CO}_2)_2$, and $\text{IBr}^-(\text{CO}_2)_3$ two-photon products and then normalizing the (constant) signal level at 100 ps to unity. Clearly, this transient is much more complicated than that observed for $\text{IBr}^-(\text{CO}_2)_{11}$. There is a sharp initial rise from 0.4 to 1 ps, then a plateau at 3–5 ps, and finally a decrease and leveling off in the signal by 10–20 ps. Data were recorded for time delays as long as 500 ps, and no significant changes in the signal intensity were observed after 20 ps. It is interesting to note that the signal at 3–5 ps actually exceeds that at 100 ps. A qualitative explanation for this behavior is given below. It is clear, however, that unlike the data for $\text{IBr}^-(\text{CO}_2)_{11}$ and $\text{IBr}^-(\text{CO}_2)_{12}$, this transient cannot be accurately fitted with a simple exponential rise. We are left, then, to make only a qualitative estimate of the absorption recovery time, as discussed below.

As shown by the filled circles in Fig. 8, a transient was also recorded for $\text{IBr}^-(\text{CO}_2)_{14}$. This transient was acquired

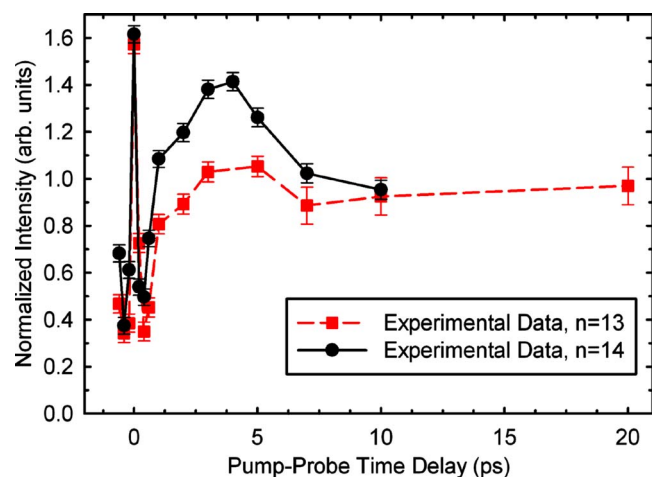


FIG. 8. (Color online) Absorption recovery transient for $\text{IBr}^-(\text{CO}_2)_{13}$ (dashed line and squares) and $\text{IBr}^-(\text{CO}_2)_{14}$ (solid line and circles). The lines are shown to guide the eye.

by summing the $\text{IBr}^-(\text{CO}_2)_2$, $\text{IBr}^-(\text{CO}_2)_3$, and $\text{IBr}^-(\text{CO}_2)_4$ two-photon products. The intensity was again normalized to unity at the signal level at 100 ps. Note that this transient is qualitatively similar to that observed for $\text{IBr}^-(\text{CO}_2)_{13}$. A sharp rise is observed from 0.4 to 1.0 ps, along with a peak at 4 ps, and a gradual decay and leveling off in the signal by 10 ps. As with $\text{IBr}^-(\text{CO}_2)_{13}$, data were taken out to a 500 ps time delay, and no significant changes in the signal level were observed at long time delays. Thus, the experiments do not confirm the predictions by theory that the absorption recovery of $\text{IBr}^-(\text{CO}_2)_{14}$ should consist of both a fast and a slow component (see Sec. III B 2). The peak of the transient at 4 ps is much more pronounced in the absorption recovery of $\text{IBr}^-(\text{CO}_2)_{14}$ than in the recovery of $\text{IBr}^-(\text{CO}_2)_{13}$, as is evidenced by the magnitude of the y scale; the signal level at 5 ps for $\text{IBr}^-(\text{CO}_2)_{13}$ is approximately 1.05, while that observed at 4 ps for $\text{IBr}^-(\text{CO}_2)_{14}$ is approximately 1.4. Interestingly, depending on the particular product detected for $\text{IBr}^-(\text{CO}_2)_{14}$, the magnitude of the peak also varied. Higher mass products gave rise to a larger peak in the transient. These observations are consistent with our picture of the absorption recovery for $\text{IBr}^-(\text{CO}_2)_{13}$ and $\text{IBr}^-(\text{CO}_2)_{14}$, as discussed below. Finally, as with $\text{IBr}^-(\text{CO}_2)_{13}$, it is impossible to get an accurate absorption recovery lifetime by fitting the data to an exponential rise. Thus, we are again left to qualitatively assign an absorption recovery lifetime, as discussed in the following paragraph.

The nonexponential behavior observed in the transients for $\text{IBr}^-(\text{CO}_2)_{13}$ and $\text{IBr}^-(\text{CO}_2)_{14}$ shown in Fig. 8 is attributed to population traversing vibrationally excited states of the ground electronic state after recombination. The absorption cross section of the $A' \leftarrow X$ transition for IBr^- peaks at 740 nm.⁴⁸ This implies that excitation from a 795 nm laser pulse, the wavelength used in these experiments, will have a greater cross section from vibrationally excited levels in the ground electronic state than from the lowest vibrational levels. Figure 9 illustrates this with a cartoon schematic of the excitation of the chromophore from the lowest vibrational level, $h\nu_{\text{asym}}$, and from an excited vibrational level, $h\nu_{\text{overshoot}}$. The sharp rise observed in the transients for n

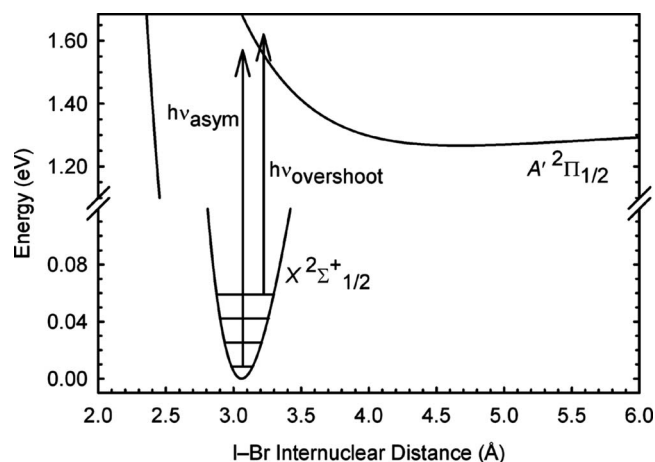


FIG. 9. Cartoon illustrating the origin of the overshoot of the asymptote for the absorption recovery of $\text{IBr}^-(\text{CO}_2)_{13,14}$. The ground-state potential is a Morse potential obtained using the experimentally determined parameters for the equilibrium bond length and vibrational frequency (Refs. 52 and 53). The excited-state potential is also a model Morse potential with the well depth chosen to match the experimentally determined value (Ref. 54) and the equilibrium bond length adjusted to illustrate the origin of the overshoot. The arrow labeled $h\nu_{\text{overshoot}}$ represents the transition giving rise to the overshoot of the asymptote, and the arrow labeled $h\nu_{\text{asym}}$ represents the transition giving rise to the asymptotic signal. Note the break in the energy scale along the y axis.

$= 13$ and 14 from 0.4 to 1.0 ps, then, is attributed to population traversing high vibrational states in the ground electronic state. The transient then peaks above the normalization point at 4 ps, at which time recombined population is traversing intermediate vibrationally excited levels. This is illustrated by the $h\nu_{\text{overshoot}}$ arrow in the figure. Finally, the transient reaches the asymptotic level at 10 ps when the population has reached low vibrational levels, as shown by the $h\nu_{\text{asym}}$ arrow. Based on this description of the transients observed for $\text{IBr}^-(\text{CO}_2)_{13}$ and $\text{IBr}^-(\text{CO}_2)_{14}$, we assign their absorption recovery lifetimes as 5(3) and 4(2) ps, respectively. This picture also supports our observation that the higher mass products for $\text{IBr}^-(\text{CO}_2)_{14}$ give rise to a larger peak in the transient because higher mass products are less likely to make it back down to the lowest vibrational levels in the ground state. Thus, they will be more prevalent in the intermediate vibrational levels which correspond to the signal responsible for the peak in the transient. We should also point out that the theoretical methods used in simulating the absorption recovery dynamics of these clusters, as outlined in Sec. III B 2, do not account for the change in the IBr^- cross section as a function of vibrational level and therefore will not reproduce the peak in the transient.

2. Simulated absorption recovery dynamics of $\text{IBr}^-(\text{CO}_2)_n$, $n=5-16$

Long time nonadiabatic MD simulations of $\text{IBr}^-(\text{CO}_2)_{5-16}$ were carried out to obtain simulated time constants for ground-state recombination. All simulations used a time step of 1 fs, while the length of simulations ranged from 20 ps for $\text{IBr}^-(\text{CO}_2)_5$ to 2 ns for $\text{IBr}^-(\text{CO}_2)_{8,10}$ with ensemble sizes ranging from 100 trajectories for $\text{IBr}^-(\text{CO}_2)_{8,10}$ to over

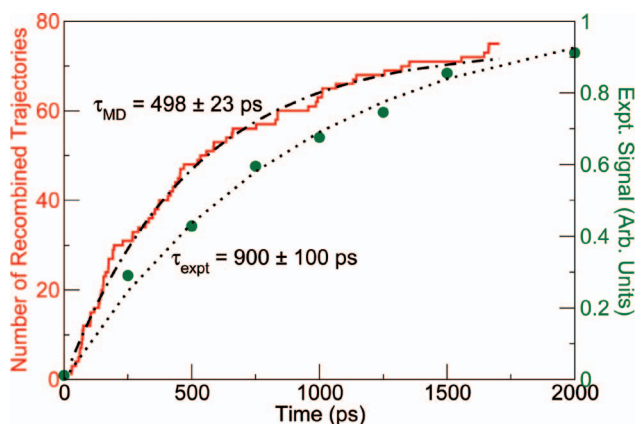


FIG. 10. (Color) Ground-state recombination dynamics for $\text{IBr}^-(\text{CO}_2)_8$. The stepped line represents theoretical results, τ_{MD} , and the dots represent experimental data, τ_{expt} . The dotted and dashed-dotted-dashed lines represent single exponential fits to the experimental and simulated data, respectively, see Eq. (2).

1700 for $\text{IBr}^-(\text{CO}_2)_5$. A trajectory was considered to have recombined when the IBr^- bond length reached 3.3 \AA on the ground state.

A few comments are in order concerning the precise relationship between the experimental signal and the simulations. In previous work,^{17,38} we simulated the absorption recovery directly using a quasiclassical energy-gap procedure. That procedure requires extremely large trajectory ensembles (since at any time, only a small fraction of the ensemble, that fraction for which the energy gap between two electronic states corresponds to the probe absorption frequency, contributes to the calculated probe signal) and is only feasible for simulation times of a few picoseconds. In the present case, we are focused on much longer timescales, so we adopt a much simpler procedure: we assume that the probe absorption is proportional to the fraction of trajectories that have recombined on the ground state. The time required for trajectories to reach the ground state is typically much longer than the timescale of vibration and of vibrational relaxation on the ground state so that we can neglect the precise location of the ground-state absorption windows.

In most cases, it was possible to fit the time dependence of the recombination with a simple exponential [Eq. (2)]. An example of this fit is provided in Fig. 10 which plots both the theoretical and experimental results along with their respective single exponential fits. The exceptions were $\text{IBr}^-(\text{CO}_2)_{14}$, which required a biexponential fit, and $\text{IBr}^-(\text{CO}_2)_{5,6}$, for which a time delay of several picoseconds elapsed before recombination began. In the latter case, the time dependence was fitted to the expression

$$N(t) = A_0 [1 - e^{-(t-t_0)/\tau}], \quad (3)$$

where the time delay t_0 is treated as an additional fit parameter. The simulated ground-state recombination times are summarized along with the experimental results in Fig. 11. Both experiment and simulation show an increase in ground-state recombination time of two to three orders of magnitude from $\text{IBr}^-(\text{CO}_2)_5$ to $\text{IBr}^-(\text{CO}_2)_{8-10}$.

The extraordinarily long relaxation times observed in both simulation and experiment for $n=8-10$ strongly sug-

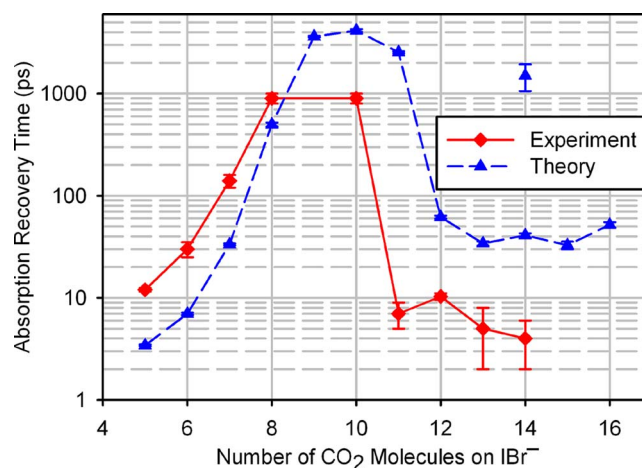


FIG. 11. (Color online) Comparison of experimental and theoretical ground-state recombination times. The solid line and diamonds represent the experimental data, and the dashed line and triangles represent the results of the theoretical calculations. The lines connecting the data points correspond to the fast component of the absorption recovery in cases where the recovery was best fit to a biexponential function. The data points not connected by a line correspond to the slow component of the absorption recovery.

gest that in the solvated molecular ion, the potential energy surface corresponding to the A' state contains a deep well. In order to elucidate the topography of this multidimensional surface, we adopt a technique used previously by our group,^{21,38} in which trajectories are analyzed in terms of two coordinates, solute bond length and a collective solvent coordinate. We define this solvent coordinate, $\Delta\Phi$, as the change in energy when a charge of $-e$ is moved from one solute atom to another. A larger absolute value of $\Delta\Phi$ represents more solvent asymmetry, Fig. 12 (bottom), while a $\Delta\Phi$ near zero represents a more symmetric solvent configuration, Fig. 12 (top). Note that, in contrast to a symmetric solute system such as $\text{I}_2^-(\text{CO}_2)_n$, $\Delta\Phi=0$ does not correspond exactly to a symmetric solvent configuration as the two solute atoms are not the same. Also, many different solute-solvent configurations correspond to the same value of $\Delta\Phi$.

While these plots allow analysis of the concerted motion

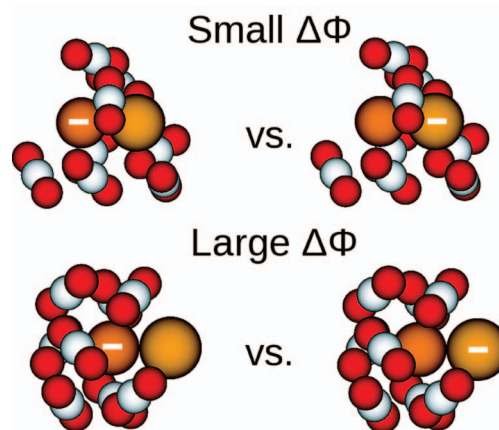


FIG. 12. (Color) Visual representation of the solvent coordinate, $\Delta\Phi$, using $\text{IBr}^-(\text{CO}_2)_8$ clusters. $\Delta\Phi$ is defined by the change in energy when the charge is transferred from the bromine atom to the iodine atom as shown on the left and right sides of the figure, respectively. A symmetric solvent configuration (top) corresponds to a small $\Delta\Phi$. An asymmetric solvent configuration (bottom) corresponds to large values of $\Delta\Phi$.

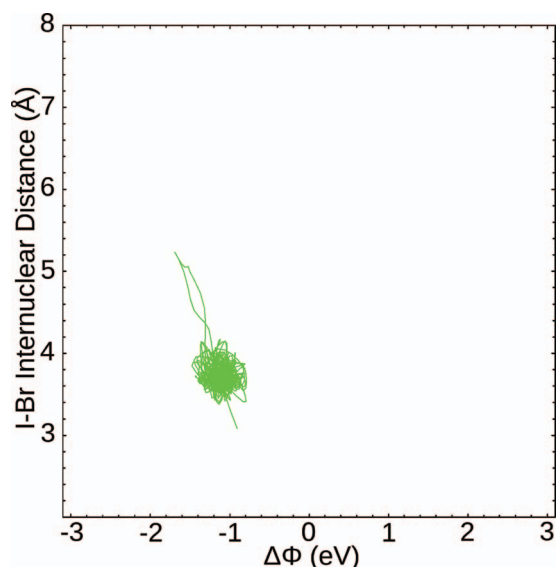


FIG. 13. (Color) Plot of solute internuclear distance vs solvent coordinate, $\Delta\Phi$, for a trapped trajectory for $\text{IBr}^-(\text{CO}_2)_8$. The green line represents trajectory dynamics on the A' state shown in Fig. 1.

of the solute and solvent over the length of the trajectory, the energy landscape has to be inferred from the limitations of this movement on the two-dimensional (2D) surface. Wells and valleys of the energy landscape are indicated by batches of trajectories that are trapped either in small, compact areas (wells) or long, slim areas (valleys) on the 2D surface. The state which a trajectory currently occupies is color coded according to the scheme used in the bare IBr^- potential energy curve, Fig. 1, where green, red, and black represent the A' , A , and X states, respectively.

To demonstrate the utility of these solvent flow plots, two examples for $\text{IBr}^-(\text{CO}_2)_8$ are presented that allow analysis of the ground-state recombination dynamics. The first of these plots, Fig. 13, is an example of a trajectory that was trapped over its 50 ps lifetime. After excitation to the A' state (the point roughly at 3 Å), the solute begins to dissociate, and the solvent becomes more asymmetric around the solute. At this point it becomes trapped in a well located at about 3.8 Å. While the solute does make an attempt to dissociate, the turning point implies the existence of a wall to dissociation as the I-Br bond length increases.

In comparison to this trapped trajectory, Fig. 14 shows one that achieves ground-state recombination. In this case, while the cluster was initially trapped in the same excited-state well, it eventually achieved a more symmetric solvent configuration, which allowed it to cross over to a configuration in which I^- is solvated (positive $\Delta\Phi$). At this point it was able to increase its bond length to a point where a nonadiabatic transition to the A state was possible (shown as a color change from green to red). After the hop was made, the trajectory quickly (on the order of a few picoseconds) hopped to the ground state and recombined in the ground-state well.

Plots like these allow us to gauge the concerted movement of both the solute and solvent on the potential energy surface. Figure 14 allows us to elucidate the mechanism behind the trapping and relaxation for smaller clusters. A con-

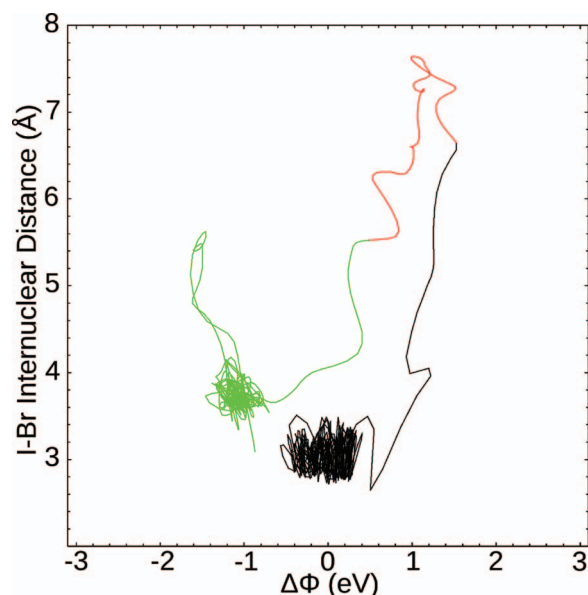


FIG. 14. (Color) Plot of solute internuclear distance vs solvent coordinate, $\Delta\Phi$, for a relaxed trajectory for $\text{IBr}^-(\text{CO}_2)_8$. Black, red, and green represent trajectory dynamics on the X , A , and A' states, respectively, as seen in Fig. 1.

certed configurational change in both solute, stretching the solute bond, and solvent geometry, a more symmetric, i.e., small $|\Delta\Phi|$, is needed to reach the configuration necessary for a nonadiabatic transition to occur (shown by the color change from green to red). To better show the location of this configurational transition state, a solvent flow plot of all 75 trajectories that relaxed to the ground state during the 2 ns runs, overlaid into one plot, is presented in Fig. 15. This plot shows that every single trajectory that eventually relaxes to the ground state must pass through a transition state located

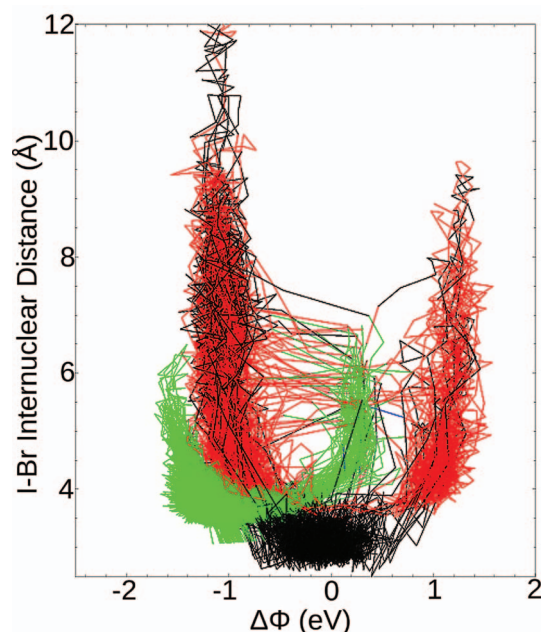


FIG. 15. (Color) Plot of solute internuclear distance vs solvent coordinate, $\Delta\Phi$, for 2 ns trajectories for $\text{IBr}^-(\text{CO}_2)_8$ that end with the IBr^- product in the ground state. Black, red, and green represent trajectory dynamics on the X , A , and A' states, respectively, as seen in Fig. 1.

roughly at $\Delta\Phi = -0.3$ eV and $R = 3.9$ Å. There appears to be a very narrow range of solvent configurations that will afford escape from the excited-state well. Furthermore, Fig. 15 also allows a more complete mapping of the energy surface seen by $\text{IBr}^-(\text{CO}_2)_8$ during its trajectories. First, the excited-state well, while concentrated around 4 Å of solute separation, is not so compact that trajectories cannot reach bond lengths of up to 6 Å. In other words, the excited state is bound, but only loosely. At longer bond lengths, the A' state seems to evolve from a single well structure to a double well structure. This seems to be crucial as it allows the clusters to reach the valley in the A' state located at zero $\Delta\Phi$ where the nonadiabatic $A' \rightarrow A$ transitions occur. Likewise, the long bond length double-valley structure extends to both the A state and ground state. As discussed in earlier^{21,38} studies of $\text{I}_2^-(\text{CO}_2)_n$, the double wells in the X and A states correspond to localized charge distributions (solvated I^- and bromine and iodine and solvated Br^-), whereas the single well on the X state at short bond lengths corresponds to a delocalized, molecular charge distribution. The delocalized distribution wins out at short separations where the chemical bonding interactions are stronger than the X^- -solvent interactions. In the A state, the chemical forces are weak for all R , so the charge remains localized at nearly all internuclear distances. Moreover, there is a very real energy barrier associated with this configurational transition state. An increase in photon energy in simulations, from 790 to 730 nm, which amounts to an increase in the kinetic energy release on the A' state from 0.29 to 0.42 eV, led to nearly all $\text{IBr}^-(\text{CO}_2)_8$ trajectories relaxing to the ground state within 50 ps, in marked contrast to the nanosecond timescale of the lower energy release simulations. This is an important point because it indicates that the origin of the nanosecond recombination timescale may have more to do with the kinetic energy release to the products than with the chemical identity of the chromophore. This idea is further supported by the fact that the experiments on $\text{I}_2^-(\text{CO}_2)_n$, which exhibited absorption recovery on the tens of picosecond timescale,^{10,12} involved more kinetic energy release to the products than the current $\text{IBr}^-(\text{CO}_2)_n$ experiments.

As shown in Fig. 11, the current $\text{IBr}^-(\text{CO}_2)_n$ simulations also show a turnaround in ground-state relaxation times at larger clusters. $\text{IBr}^-(\text{CO}_2)_{12}$ appears to be the critical size after which relaxation times return to the sub-100-ps range. This recovery is due to the fact that for $n > 12$ the cluster's excited-state solvent configurations are more symmetric. Figure 16 demonstrates that $n = 12$ corresponds to an especially labile solvent configuration: the range of $\Delta\Phi$ values over the ensemble is very large, allowing for easy access to both Br-solvated ($-\Delta\Phi$) and I-solvated ($+\Delta\Phi$) configurations at a longer solute bond length. For $n > 12$, $\Delta\Phi$ is mostly positive, so these trajectories start out with solvated I. The larger clusters then have easy access to the regions of the excited-state potential surface where electronic quenching can occur.

Overall, the experiments and simulations show similar qualitative trends, although the quantitative discrepancies are obviously large—hardly a surprise given the extraordinarily long timescales involved. From $n = 5$ to 9, the time constant for recombination increases rapidly and, to a first approximation, exponentially with cluster size, after which it turns

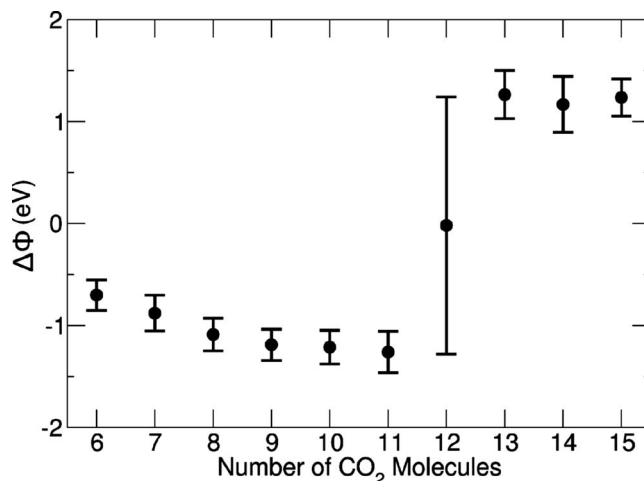


FIG. 16. Average solvent coordinate, $\Delta\Phi$, of the excited-state well in $\text{IBr}^-(\text{CO}_2)_{6-15}$ trajectory simulations. Error bars represent one standard deviation of the mean.

around and finally levels off at about $n = 13$. (We note again that this turnaround was predicted by theory before it was confirmed by experiment.) One remaining puzzle is $\text{IBr}^-(\text{CO}_2)_{14}$. As shown in Fig. 17, the simulations of this cluster demonstrated a strongly biexponential relaxation, with one time constant being very short (40 ps) and the other much longer (> 1 ns). In the simulation these two time constants could be clearly identified as arising from portions of the ensemble that were or were not trapped at the beginning of the simulation. This behavior persisted when the initial excitation wavelength was decreased to 730 nm (corresponding to an additional 0.13 eV of initial kinetic energy). However, the experimental results show no evidence for multiple timescale relaxation for $\text{IBr}^-(\text{CO}_2)_{14}$ and, at most, hint at the possibility of two populations for $\text{IBr}^-(\text{CO}_2)_{11}$. This discrepancy is as yet unresolved.

IV. DISCUSSION

The principal results of the experiments and simulations are presented in Figs. 6, 11, and 12 and may be summarized as follows:

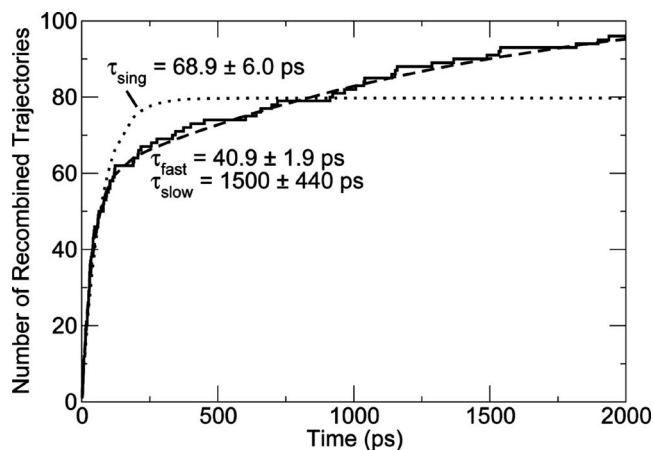


FIG. 17. Comparison of single and biexponential fits to the ground-state recombination trajectories of $\text{IBr}^-(\text{CO}_2)_{14}$. The solid line represents the theoretical results. The dotted and dashed lines are single and biexponential fits, respectively. The corresponding constants are also labeled. The ensemble is composed of one hundred 3 ns trajectories.

- (i) In these clusters, recombination is a highly efficient process in the sense that given enough time, the probability of recombination is high. It occurs to a measurable degree in clusters having as few as two solvent molecules and reaches 100% for clusters having eight or more solvent molecules, significantly less than a closed solvent shell. This is very similar to the behavior seen for $\text{I}_2^-(\text{CO}_2)_n$ clusters.^{10,12}
- (ii) While recombination is efficient, it is not necessarily fast, and the long time probability of recombination is not simply related to the rate. The timescale for recombination increases with increasing cluster size, up to $n=10$, and then decreases as n increases further. This is drastically different from the behavior seen in I_2^- clusters.¹⁰ In particular, the recombination times for $n=8-10$ are orders of magnitude longer than those seen in the homonuclear system.
- (iii) The solvent coordinate $\Delta\Phi$ plays a decisive role in recombination. The timescale for recombination is strongly correlated with the early-time distribution of $\Delta\Phi$ (Fig. 16), and trajectories that lead to recombination all follow similar pathways when plotted in $(r, \Delta\Phi)$ space (Figs. 14 and 15).

The increase in recombination times for $n=5-10$ appears to be roughly exponential with n , which strongly suggests that the recombination mechanism involves an activated process. Figures 12–15, in turn, elucidate the molecular origin of this process: recombination requires a collective motion of the solvent cage from the vicinity of the Br atom to that of the I atom. Collecting together the observations detailed in Sec. III, we can present a coherent description of the excitation, dissociation, and recombination processes.

In clusters having five to ten solvent molecules, absorption of a photon leads to an excited state in which the charge is predominantly localized on the Br atom (in contrast to the bare chromophore). The solvent molecules stabilize this charge distribution, more so since the I–Br bond is extended in this excited state. Increasing the number of solvent molecules increases the degree of stabilization, thereby lowering the free energy of the excited-state “well.” After a sufficiently long time, however, thermal fluctuations carry the solvent cage close to a symmetric geometry. The charge can then transfer to the iodine atom, and the solvent then reorganizes so as to stabilize this charge distribution. This solvent-driven adiabatic electron transfer event is the rate-determining step in the recombination mechanism. The well in the excited-state surface corresponding to solvated I^- is energetically close to a barrier in a lower lying excited state, however, so nonadiabatic transitions to this state and from it to the ground state are rapid. Once on the lower states, the chromophore can either dissociate (in small clusters) or recombine (in large clusters).

In clusters having more than ten solvent molecules, a further increase in n does not further stabilize the Br-localized configuration, since the additional solvent molecules add to the I side of the anionic chromophore. Indeed, one can expect that by stabilizing the I^- localized configura-

tion, the additional solvents may actually pull down the barrier to solvent reorganization. This is particularly easy to see if one regards the trajectory patterns mapped out by Figs. 13–15 as delineating the topographic features of a *free-energy* surface. The free-energy barrier to solvent reorganization has both an energetic and an entropic component. In the largest clusters, both components are small, since a small amount of energy is required to move any given solvent molecule, and only a few solvent molecules need to be moved in order for the solvent cage to reach a configuration at which nonadiabatic electronic quenching can occur.

We return, finally, to the conundrum with which we opened this paper: How does it come about that the branching ratio and the rate constant for recombination do not track one another? The answer is that the two processes are determined by the dynamics on different potential surfaces. Except in the very smallest clusters ($n < 4$) there is essentially no dissociation on the initially excited surface. Instead, the simulations imply that the branching between dissociation and recombination takes place on the *A* and *X* surfaces, following solvent reorganization and electronic quenching. As n increases from 5 to 10, the timescales for both dissociation and recombination increase because the solvated Br^- configuration becomes more stable. Once solvent reorganization and electronic quenching have occurred, however, the larger clusters can more effectively cage the fragments on the lower surface.

V. SUMMARY AND CONCLUSIONS

Experimental studies and nonadiabatic MD simulations of the photodissociation and recombination of size-selected $\text{IBr}^-(\text{CO}_2)_n$ anionic clusters following excitation in the near IR have been carried out. The simulations rely on an effective Hamiltonian model that accounts, in a self-consistent fashion, for the interaction between the polarizable charge distribution on the anionic chromophore and the electrostatic forces due to the solvent molecules. The surprising results of recent experimental studies⁴⁹ of this system—recombination times that increase with cluster size, resulting in timescales of the order of nanoseconds in clusters having eight to ten solvent molecules—are reproduced by the simulations, which furthermore predict that the timescale decreases again as the cluster size is increased further. New experimental results, presented for the first time in this paper, confirm this latter prediction. A detailed analysis of the simulation trajectories leads to a comprehensive physical explanation for the experimental trends: recombination is found to be an activated process, with the rate-determining step being the collective motion of the solvent cage from a configuration that stabilizes a charge localized on Br^- to one that favors I^- .

ACKNOWLEDGMENTS

We gratefully acknowledge support from the National Science Foundation, Awards CHE0809391 and PHY 0551010, and the Air Force Office of Scientific Research, Award FA9550-06-1-0066. We also thank Dr. Joseph Fowler, Dr. Nikki Delaney, Dr. James Faeder, and Dr. Paul Maslen for their discussions on all aspects of this work.

- ¹D. M. Neumark, *Annu. Rev. Phys. Chem.* **52**, 255 (2001).
- ²D. M. Neumark, *J. Chem. Phys.* **125**, 132303 (2006).
- ³D. M. Neumark, *Phys. Chem. Chem. Phys.* **7**, 433 (2005).
- ⁴A. Sanov and W. C. Lineberger, *Phys. Chem. Chem. Phys.* **6**, 2018 (2004).
- ⁵J. Simons, *J. Phys. Chem. A* **112**, 6401 (2008).
- ⁶P. L. Houston, *Chemical Kinetics and Reaction Dynamics* (McGraw-Hill, New York, 2001).
- ⁷M. E. Nadal, P. D. Kleiber, and W. C. Lineberger, *J. Chem. Phys.* **105**, 504 (1996).
- ⁸S. Nandi, A. Sanov, N. Delaney, J. Faeder, R. Parson, and W. C. Lineberger, *J. Phys. Chem.* **102**, 8827 (1998).
- ⁹J. M. Papanikolas, J. R. Gord, N. E. Levinger, D. Ray, V. Vorsa, and W. C. Lineberger, *J. Phys. Chem.* **95**, 8028 (1991).
- ¹⁰J. M. Papanikolas, V. Vorsa, M. E. Nadal, P. J. Campagnola, H. K. Buchenau, and W. C. Lineberger, *J. Chem. Phys.* **99**, 8733 (1993).
- ¹¹A. Sanov, T. Sanford, L. J. Butler, J. Vala, R. Kosloff, and W. C. Lineberger, *J. Phys. Chem. A* **103**, 10244 (1999).
- ¹²V. Vorsa, S. Nandi, P. J. Campagnola, M. Larsson, and W. C. Lineberger, *J. Chem. Phys.* **106**, 1402 (1997).
- ¹³N. Delaney, J. Faeder, P. E. Maslen, and R. Parson, *J. Phys. Chem. A* **101**, 8147 (1997).
- ¹⁴N. Delaney, J. Faeder, and R. Parson, *J. Chem. Phys.* **111**, 651 (1999).
- ¹⁵J. Faeder, N. Delaney, P. E. Maslen, and R. Parson, *Chem. Phys. Lett.* **270**, 196 (1997).
- ¹⁶J. Faeder, N. Delaney, P. E. Maslen, and R. Parson, *Chem. Phys.* **239**, 525 (1998).
- ¹⁷R. Parson, J. Faeder, and N. Delaney, *J. Phys. Chem. A* **104**, 9653 (2000).
- ¹⁸V. Dribinski, J. Barbera, J. P. Martin, A. Svendsen, M. A. Thompson, R. Parson, and W. C. Lineberger, *J. Chem. Phys.* **125**, 133405 (2006).
- ¹⁹T. Sanford, S.-Y. Han, M. A. Thompson, R. Parson, and W. C. Lineberger, *J. Chem. Phys.* **122**, 054307 (2005).
- ²⁰P. E. Maslen, J. Faeder, and R. Parson, *Chem. Phys. Lett.* **263**, 63 (1996).
- ²¹N. Delaney, Ph.D. thesis, University of Colorado, 1999.
- ²²D. W. Boo, Y. Ozaki, L. H. Andersen, and W. C. Lineberger, *J. Phys. Chem. A* **101**, 6688 (1997).
- ²³N. E. Levinger, D. Ray, M. L. Alexander, and W. C. Lineberger, *J. Chem. Phys.* **89**, 5654 (1988).
- ²⁴V. Vorsa, P. J. Campagnola, S. Nandi, M. Larsson, and W. C. Lineberger, *J. Chem. Phys.* **105**, 2298 (1996).
- ²⁵W. C. Wiley and I. H. McLaren, *Rev. Sci. Instrum.* **26**, 1150 (1955).
- ²⁶A. Sanov, T. Sanford, S. Nandi, and W. C. Lineberger, *J. Chem. Phys.* **111**, 664 (1999).
- ²⁷H. J. Werner, P. J. Knowles, R. Lindh *et al.*, MOLPRO, Version 2002.6, a package of *ab initio* programs, 2003 (<http://www.molpro.net>).
- ²⁸H. Stoll, B. Metz, and M. Dolg, *J. Comput. Chem.* **23**, 767 (2002).
- ²⁹H. Stoll, personal communication (2002).
- ³⁰P. J. Knowles and H. J. Werner, *Chem. Phys. Lett.* **145**, 514 (1988).
- ³¹P. J. Knowles and H. J. Werner, *Theor. Chim. Acta* **84**, 95 (1992).
- ³²H. J. Werner and P. J. Knowles, *J. Chem. Phys.* **89**, 5803 (1988).
- ³³P. J. Knowles and H. J. Werner, *Chem. Phys. Lett.* **115**, 259 (1985).
- ³⁴H. J. Werner and P. J. Knowles, *J. Chem. Phys.* **82**, 5053 (1985).
- ³⁵A. Berning, M. Schweizer, H. J. Werner, P. J. Knowles, and P. Palmieri, *Mol. Phys.* **98**, 1823 (2000).
- ³⁶P. E. Maslen, J. Faeder, and R. Parson, *Mol. Phys.* **94**, 693 (1998).
- ³⁷N. Delaney, J. Faeder, and R. Parson, *J. Chem. Phys.* **111**, 651 (1999).
- ³⁸N. Delaney, J. Faeder, and R. Parson, *J. Chem. Phys.* **111**, 452 (1999).
- ³⁹A. J. Stone, *The Theory of Intermolecular Forces* (Oxford, New York, 1996).
- ⁴⁰C. S. Murthy, S. F. Oshea, and I. R. McDonald, *Mol. Phys.* **50**, 531 (1983).
- ⁴¹I. Yourshaw, Y. X. Zhao, and D. M. Neumark, *J. Chem. Phys.* **105**, 351 (1996).
- ⁴²H. C. Andersen, *J. Comput. Phys.* **52**, 24 (1983).
- ⁴³S. Hammes-Schiffer and J. C. Tully, *J. Chem. Phys.* **101**, 4657 (1994).
- ⁴⁴J. C. Tully, *J. Chem. Phys.* **93**, 1061 (1990).
- ⁴⁵W. H. Press, S. A. Teukolsky, W. T. Vetterling, and B. P. Flannery, *Numerical Recipes in C: The Art of Scientific Computing*, 2nd ed. (Cambridge University Press, New York, 1992).
- ⁴⁶J. M. Papanikolas, V. Vorsa, M. E. Nadal, P. J. Campagnola, H. K. Buchenau, and W. C. Lineberger, *J. Chem. Phys.* **99**, 8733 (1993).
- ⁴⁷J. Faeder, Ph.D. thesis, University of Colorado, 1998.
- ⁴⁸T. Sanford, Ph.D. thesis, University of Colorado, 2004.
- ⁴⁹V. Dribinski, J. Barbera, J. P. Martin, A. Svendsen, M. A. Thompson, R. Parson, and W. C. Lineberger, *J. Chem. Phys.* **125**, 133405 (2006).
- ⁵⁰C. E. Moore, *Atomic Energy Levels* (National Bureau of Standards, Washington, D.C., 1949).
- ⁵¹*CRC Handbook of Chemistry and Physics*, 66th ed. (CRC, Boca Raton, 1985).
- ⁵²R. J. Le Roy, "LEVEL 7.7: A computer program for solving the radial Schrödinger equation for bound and quasibound levels," University of Waterloo Chemical Physics Research Report No. CP-661, 2005 (see <http://leroy.uwaterloo.ca/programs/>).
- ⁵³L. Sheps, E. Miller, and W. C. Lineberger, "Time resolved photoelectron spectra of $\text{IBr}^-(\text{CO}_2)_n$: Energetics and solvent-induced curve-crossings observed in real time" (unpublished).
- ⁵⁴R. Mabbs, K. Pichugin, and A. Sanov, *J. Chem. Phys.* **122**, 174305 (2005).